

Spin distribution of binary black holes formed in open clusters

Jun Kumamoto,¹  Michiko S. Fujii,¹ Alessandro A. Trani,² and Ataru Tanikawa²

¹ Department of Astronomy, Graduate School of Science, The University of Tokyo, 7-3-1 Hongo, Bunkyo-ku, Tokyo 113-0033, Japan

² Department of Earth Science and Astronomy, College of Arts and Sciences, The University of Tokyo, 3-8-1 Komaba, Meguro-ku, Tokyo 153-8902, Japan

Accepted XXX. Received YYY; in original form ZZZ

ABSTRACT

We performed direct N-body simulations of open clusters with four different metallicities. To investigate the effective spins of merging binary black holes (BBHs) originated from these open clusters, we calculated the spin evolution of Wolf-Rayet (WR) stars with close companion stars (BBH progenitors), taking into account stellar wind mass loss and tidal spin-up of the WR stars. We found that BBH progenitors with smaller semi-major axes evolve to merging BBHs with greater effective spins because of strong tidal forces. In the local Universe, about 16% of merging BBHs get effective spins larger than 0.1 even if BHs and their progenitors do not get spin angular momenta other than tidal forces exerted by their companion stars. If we assume that WR stars have flat and isotropic distribution of dimensionless spins just after common envelope phases, the effective spin distribution of merging BBHs is similar to that inferred from gravitational wave observations with LIGO and Virgo.

Key words: gravitational waves – methods: numerical – stars: black holes

1 INTRODUCTION

The recent detections of gravitational waves with LIGO and Virgo have revealed many mergers of two stellar-mass black holes (BHs) (e.g. Abbott et al. 2019a, 2020). Prior to their detection, it was not expected that there would be so many massive ($>15 M_{\odot}$) merging binary BHs (BBHs). Numerous scenarios have been suggested to explain the formation process of these BBHs, but their origin is still unclear.

One of the main scenarios is via common envelope and mass transfer evolution of isolated field binaries (e.g. Tutukov et al. 1973; Bethe & Brown 1998; Dominik et al. 2012; Kinugawa et al. 2014; Belczynski et al. 2016, 2020; Giacobbo et al. 2018; Bavera et al. 2020; Tanikawa et al. 2020a,b). The other major scenarios are the dynamical formation due to three-body encounters in globular clusters (e.g. Portegies Zwart & McMillan 2000; O’Leary et al. 2006; Sadowski et al. 2008; Downing et al. 2010, 2011; Banerjee et al. 2010; Tanikawa 2013; Bae et al. 2014; Rodriguez et al. 2015, 2016; Fujii et al. 2017; Park et al. 2017; Askar et al. 2017; Hong et al. 2018; Zevin et al. 2019; Antonini & Gieles 2020; Kremer et al. 2020; Wang et al. 2021), open cluster (or young star cluster) (e.g. Ziosi et al. 2014; Goswami et al. 2014; Mapelli 2016; Banerjee 2017, 2018a,b; Rastello et al. 2019; Di Carlo et al. 2019; Kumamoto et al. 2019, 2020; Bouffanais et al. 2019; Banerjee 2021; Trani et al. 2021) or galactic nuclei (e.g. O’Leary et al. 2009; Antonini & Rasio 2016; Hoang et al. 2018; Hamers et al. 2018; McKernan et al. 2018; Hoang et al. 2019; Arca-Sedda & Capuzzo-Dolcetta 2019;

Tagawa et al. 2020; Trani 2020; Arca Sedda 2020). However, the origin of merging BBHs has been under debate.

In Kumamoto et al. (2019, hereafter Paper I), we performed N-body simulations for open clusters with half-mass densities of $10^4 M_{\odot} \text{pc}^{-3}$, and found a new channel for formation of BBHs merging within the Hubble time. In open clusters, despite the short lifetimes of massive main-sequence (MS) stars, they can form binaries due to three-body interaction before they evolve to BHs because the core-collapse time of open cluster is shorter than the lifetime of massive MS stars. These binaries evolve to BBHs merging within the Hubble time via common envelope evolution. In Kumamoto et al. (2020, hereafter Paper II), we estimated the local merger rate density of BBHs formed in open clusters to be $\sim 70 \text{yr}^{-1} \text{Gpc}^{-3}$ using the results of our N-body simulations of open clusters with four different metallicity models. This result is comparable to the merger rate density expected from the gravitational wave observation with LIGO and Virgo (Abbott et al. 2019b).

The effective spin, χ_{eff} , is one of important parameters for discussing the formation scenario of BBHs. The distribution of χ_{eff} estimated from the detection of gravitational waves show that most of BBHs have small positive and negative χ_{eff} (Abbott et al. 2019a; The LIGO Scientific Collaboration et al. 2020).

One possible scenario for the origin of BH spin is tidal spin-up of Wolf-Rayet (WR) stars before they evolve into BHs. Several previous studies showed that WR stars can be spun up if they have very close companion stars (Kushnir et al. 2017; Hotokezaka & Piran 2017; Piran & Piran 2020; Belczynski et al. 2020).

In this paper, we investigate the effective spins of BBHs formed in open clusters. For the members of BBHs formed in our simulations, we calculate the spin evolution of WR stars before they evolve into BHs. We find that even if we assume that WR stars have

* E-mail: kumamoto@astron.s.u-tokyo.ac.jp

Table 1. Models.

	$M_{\text{cl,ini}} [M_{\odot}]$	Z	N_{run}
Model Z0002	2.5×10^3	0.002	360
Model Z0005	2.5×10^3	0.005	500
Model Z001	2.5×10^3	0.01	1000
Model Z002	2.5×10^3	0.02	1000

zero spin angular momenta just after common envelope evolution, some BBH progenitors with small semi-major axes evolve to BBHs with χ_{eff} larger than 0.1. In subsolar-metallicity cases, some BBHs formed in more metal-rich clusters have lower masses and higher χ_{eff} . In the solar-metallicity case, our simulations show that there is no BBH with χ_{eff} larger than 0.1.

The structure of this paper is as follows. Our simulation methods and models are described in Section 2. We show our spin evolution model of WR stars (BH progenitors) to calculate effective spins of BBHs in Section 3. In Section 4, we investigate and discuss the distribution of the effective spins of BBHs formed in our open cluster simulations. We make a conclusion in Section 5.

2 SIMULATIONS

We analyze the results of N -body simulations for open clusters with different four metallicities ($Z = 0.002, 0.005, 0.01, 0.02$) performed in Paper II. A summary of these simulations is following.

2.1 Initial conditions

We have set up four cluster models. Table 1 gives an overview of the models. The initial cluster mass ($M_{\text{cl,ini}}$) is $2500 M_{\odot}$. The number of runs (N_{run}) depends on metallicity. Since we expect that more metal-rich clusters have a smaller number of heavy BHs due to the strong stellar wind mass loss, we performed a larger number of runs for more metal-rich clusters for statistics (see also Section 2.3).

We adopt the Plummer profile as the initial density distribution of our open cluster models (Plummer 1911);

$$\rho(r) = \frac{3M_{\text{cl,ini}}}{4\pi r_p^3} \left(1 + \frac{r^2}{r_p^2}\right)^{-5/2}, \quad (1)$$

$$r_p = (2^{2/3} - 1)^{1/2} r_{\text{hm}}, \quad (2)$$

where r_{hm} is a half-mass radius. In all our models, the half-mass radii are set to be 0.31 pc. In this case, the initial half-mass densities ($\rho_{\text{hm}} = 3M_{\text{cl,ini}}/8\pi r_{\text{hm}}^3$) are equal to $10^4 M_{\odot} \text{pc}^{-3}$. This value is higher than half-mass densities of currently observed open clusters. However, the initial density of star clusters is likely higher than the currently observed one (Marks & Kroupa 2010; Portegies Zwart et al. 2010). The observed mass and half-mass density of young massive clusters are typically $\sim 10^4 M_{\odot}$ and $10^{1-4} M_{\odot} \text{pc}^{-3}$, respectively (see Figure 2 of Portegies Zwart et al. 2010). Among these clusters, younger clusters tend to have higher densities, and the ages of youngest clusters are about 2 Myr, which is younger than the lifetime of massive MS stars. The half-mass densities of these youngest clusters are about $10^4 M_{\odot} \text{pc}^{-3}$. Therefore, we use this value for initial half-mass density.

As the initial stellar mass function, we adopted the Kroupa (2001) initial mass function with a lower mass limit of $m_{\text{min}} = 0.08 M_{\odot}$ and an upper mass limit of $m_{\text{max}} = 150 M_{\odot}$. This leads to

an average stellar mass of $\langle m \rangle = 0.586 M_{\odot}$. Thus, the initial number of particles $N_{\text{ini}} = M_{\text{cl,ini}}/\langle m \rangle$ is 4266.

In our model, the half-mass relaxation time is calculated with the following equation:

$$t_{\text{rh}} \sim 0.711 \frac{N}{\log(0.4N)} \left(\frac{\rho_{\text{hm}}}{M_{\odot} \text{pc}^{-3}}\right)^{-0.5} \text{Myr}. \quad (3)$$

The core-collapse time is proportional to the relaxation time, and the proportional factor depends on the maximum and average masses of stars in the system. In our models, we obtain

$$t_{\text{cc}} \sim 0.07 t_{\text{rh,ini}} \sim 0.7 \text{Myr} \quad (4)$$

(Gürkan et al. 2004; Fujii & Portegies Zwart 2014). Since most of BBHs are formed within a few hundred Myr, tidal disruptions of the cluster due to the external tidal field are not significant in this short period. Therefore, we do not assume any external tidal force in our simulations.

We do not assume primordial binaries. In Paper I, we argued that primordial binaries do not significantly affect the merger rate of BBHs formed in open clusters. This is because merging BBHs (or their progenitors) are dynamically formed even if there is no primordial binary. In addition, previous studies have shown that the number of BBH mergers from stellar clusters per solar mass unit is about 10^{-4} – $10^{-6} M_{\odot}^{-1}$, independently of metallicity or primordial binary fraction (e.g. Ziosi et al. 2014; Di Carlo et al. 2019; Kumamoto et al. 2020). Given the modest mass ($\sim 2500 M_{\odot}$) of open clusters, primordial binaries can not substantially increase the production rate of BBHs in open clusters.

2.2 N-body simulations

We use a direct N -body simulation code, NBODY6++GPU (Wang et al. 2015), which is an MPI-parallelised and GPU enabled version of NBODY6 (Aarseth 1999). The motions of individual stars are calculated using a fourth-order Hermite scheme (Makino & Aarseth 1992). The closer binaries have time steps much smaller than the time-scale of the evolution of open clusters. Such closer binaries are integrated using KS regularization (Kustaanheimo & Stiefel 1965; Mikkola & Aarseth 1993).

Our simulations are performed using GPU cluster SGI Rackable C1102-GP8 (Reedbush-L) in the Information Technology Center, The University of Tokyo.

2.3 Stellar evolution

The evolution of stellar radius, mass, and luminosity are calculated using a stellar evolution model, SSE (Hurley et al. 2000). We use updated mass loss model (Belczynski et al. 2010), which is contained in the latest version of NBODY6. For binary evolution, NBODY6++GPU contains a binary evolution model (Tout et al. 1997), which is an algorithm for rapid evolution binary star following the common envelope and mass transfer. We set a common envelope efficiency parameter, α , to be 1/3. The BH mass also strongly depends on metallicity. More metal-rich stars evolve into less massive BHs because of the stronger stellar wind (See Figure 1. of Paper II).

The natal kicks caused by asymmetric supernovae explosion are not included in our simulation for simplification. The natal kicks may affect to the formation rate of BBHs (Tanikawa 2013), however, most BHs are retained in clusters (Morscher et al. 2013). Even if a fraction of BHs are ejected from star clusters due to the natal kicks, BBHs are hardened not only by the rest of BHs but also the other massive stars.

3 SPIN EVOLUTION MODEL

We describe here how BHs get their spin angular momenta in our model. Figure 1 shows the schematic diagram of BBH formation with spinning BHs. Two massive stars form a binary star through dynamical interactions. The primary star evolves to a post MS star, and fills its Roche lobe. Then, the primary star drives common envelope evolution, loses its envelope, and becomes a WR star. The WR star is tidally spun up by the secondary star, and collapses to a spinning BH. The secondary star can evolve to a spinning BH through the same mechanism. BH spins are higher, and more aligned to binary angular momentum vector as binary separations are smaller just after common envelope evolution. Note that BHs can be non-spinning if the binary separations are not sufficiently small.

We calculate the spin evolution of a WR star just after common envelope evolution, taking into account tidal spin-up by its companion star, and stellar wind mass loss of the WR star itself. We use the simple model adopted by Hotokezaka & Piran (2017) and Piran & Piran (2020). We outline the model here. We define the stellar dimensionless spin, projected onto the binary angular momentum vector, as

$$\chi = \frac{c}{GM^2} \mathbf{S} \cdot \frac{\mathbf{L}}{|\mathbf{L}|}, \quad (5)$$

where c , G , M , \mathbf{S} and \mathbf{L} are the speed of light, the gravitational constant, a stellar mass, a stellar spin angular momentum vector, and a binary angular momentum vector, respectively. The dimensionless spin of a WR star, $\chi_*(t)$, evolves as follows:

$$\frac{d\chi_*(t)}{dt} = \frac{(\chi_{\text{syn}} - \chi_*(t))^{8/3}}{t_{\text{syn}}} - \frac{\chi_*(t)}{t_w}. \quad (6)$$

The first and second terms on the right-hand side represent the effects of the tidal spin-up and the stellar wind, respectively. Here, t_{syn} is the timescale for the WR star to become tidally synchronized (in the absence of winds), and it is given by

$$t_{\text{syn}} \sim 10q^{-1/8} \left(\frac{1+q}{2q} \right)^{31/24} \left(\frac{t_c}{1 \text{ Gyr}} \right)^{17/8} \text{ Myr}, \quad (7)$$

where q is the mass ratio of the WR star to its companion. The timescale t_c is the merger time of the binary through gravitational wave radiation:

$$t_c \sim 10 \left(\frac{2q^2}{1+q} \right) \left(\frac{a}{44R_\odot} \right)^4 \left(\frac{M_*}{30M_\odot} \right)^{-3} \text{ Gyr}, \quad (8)$$

where a is the semi-major axis of the binary, and M_* is the WR mass. We suppose that the binary has a circular orbit, since it experiences common envelope evolution. Tides drive the stellar spin towards the synchronization value χ_{syn} , expressed as

$$\chi_{\text{syn}} \sim 0.5q^{1/4} \left(\frac{1+q}{2} \right)^{1/8} \left(\frac{\epsilon}{0.075} \right) \left(\frac{R_*}{2R_\odot} \right)^2 \left(\frac{M_*}{30M_\odot} \right)^{-13/8} \left(\frac{t_c}{1 \text{ Gyr}} \right)^{-3/8}, \quad (9)$$

$$\epsilon = \frac{I_*}{M_* R_*^2}, \quad (10)$$

where R_* and I_* are the radius and inertia of the WR star, respectively. In this work, we set ϵ to be 0.15. The timescale of stellar wind, t_w , is another parameter which we have to take into account. The WR star loses its spin angular momentum through stellar winds with this timescale. We assume that t_w corresponds to the spin loss rate;

$$t_w = \frac{\chi_*(t)}{\dot{\chi}_*(t)}. \quad (11)$$

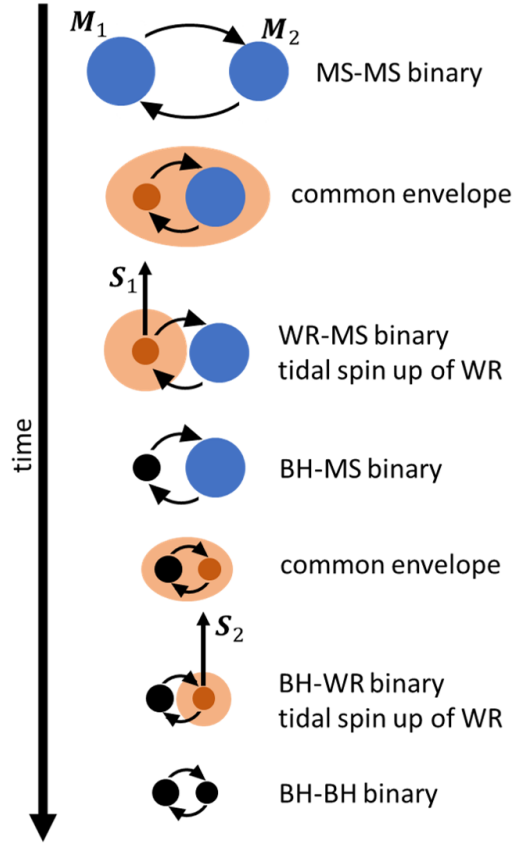


Figure 1. Schematic diagram of BBH formation with spinning BHs.

The WR star finally collapses to the primary or secondary BHs in a BBH, respectively. We can obtain the effective spin of the BBH, such that

$$\chi_{\text{eff}} = \frac{M_1 \chi_1 + M_2 \chi_2}{M_1 + M_2}, \quad (12)$$

where M_1 and M_2 are the masses of the primary and secondary BHs, respectively, and χ_1 and χ_2 are the dimensionless spins of the primary and secondary BHs.

We use two different models for the distribution of initial stellar dimensionless spins just after common envelope evolution. First, we assume that initial dimensionless spins are zero, i.e. $\chi_*(0) = 0$ for all stars. The dimensionless spins of BHs (χ_1 and χ_2) are obtained only by integrating equation (6) as they evolve from WR stars to BHs. Results in this case are shown in Sections 4.1 and 4.2. In Section 4.3, we also show the distribution of χ_{eff} in the case that the distribution of initial dimensionless spins follows a flat isotropic model, which means that the magnitude of the stellar dimensionless spin just after the common envelope is assumed to be randomly flat between 0 and 1 and the direction of the spin angular momentum vector is isotropic. We set t_w to be 1.0 Myr as our standard model. We also perform simulations with $t_w = 0.5$ and 3 Myr in Section 4.3 and compare the distribution of the effective spins for each model.

We do not take into account tidal interactions during MS and post MS phases, since they lose a large fraction of their spin angular momenta through common envelope evolution. We do not consider that BHs get spin angular momenta, accreting masses from their companions, because BHs accrete little mass in our simulations. We assume that WR stars do not lose spin angular momenta.

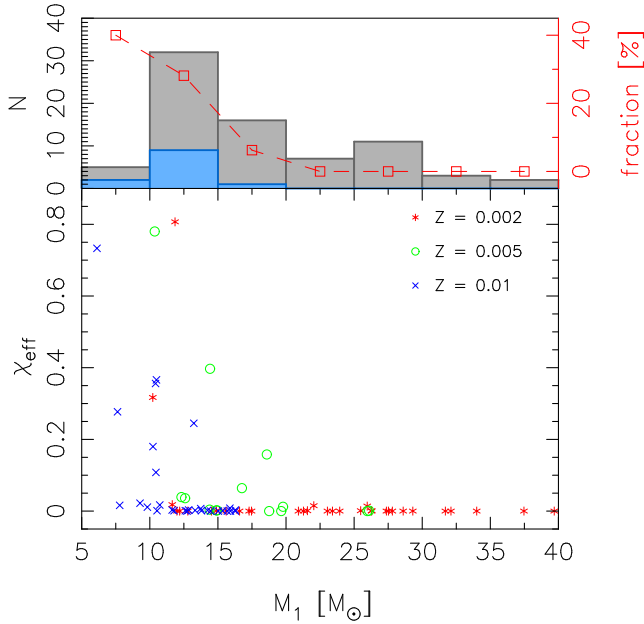


Figure 2. The bottom panel shows the distribution of the effective spins as a function of the primary mass of BBHs in the case of the zero initial dimensionless spins model. The different point types indicate different metallicities. Histograms in the top panel show the number of merging BBHs in each primary mass bin. The width of the bins is equal to $5M_{\odot}$. Grey and blue histograms show the number of BBHs with smaller and larger effective spins than 0.1. The red line with square points shows the fraction of BBHs with $\chi_{\text{eff}} > 0.1$ in each bin.

4 RESULTS AND DISCUSSION

4.1 Relation between spin and BBH properties

We obtained in total ~ 300 – 1000 BBHs ejected from clusters for four different metallicity models, however, the number of BBHs merged within 14 Gyr (hereafter, merging BBHs) is only 7–37 for each metallicity model. Here, we assume that $\chi_*(0) = 0$ for all stars, and calculate the evolution of effective spins for these merging BBHs.

Table 2 shows the number of all merging BBHs and those with $\chi_1 > 0.1$, $\chi_2 > 0.1$, and $\chi_{\text{eff}} > 0.1$ for each metallicity. For Model Z002, there is no BBH with $\chi_1 > 0.1$, $\chi_2 > 0.1$ or $\chi_{\text{eff}} > 0.1$. This is because merging BBHs are formed through three-body interactions after BH formation (See Paper II). As described in Section 3, we consider that only BH progenitors can be tidally spun up by their companions just after common envelope phases. After they evolve to BHs, they can not be tidally spun up by their companions.

Bottom panels in Figure 2, 3 and 4 show the distribution of χ_{eff} as a function of M_1 , t_{GW} (BBH merger time through gravitational wave radiation) and q for each metallicity. Grey and blue histograms in the top panel show the number of BBHs with smaller and larger effective spins than 0.1. Red dashed lines with red square points in top panels show the fraction of BBHs with $\chi_{\text{eff}} > 0.1$ in each histogram bin.

Note that the number of simulation runs is different for each metallicity model. Consequently, the spin distribution does not reflect the actual distribution of merging BBHs in the local Universe. This result only describes a rough trend in the spin distribution.

In Figure 2, our results show that only less massive BBHs ($M_1 \lesssim 20M_{\odot}$) have larger effective spins than 0.1. This result is interpreted as follows. Lower-mass BHs form from lower-mass WR stars. Such lower-mass WR stars are in binaries with smaller semi-

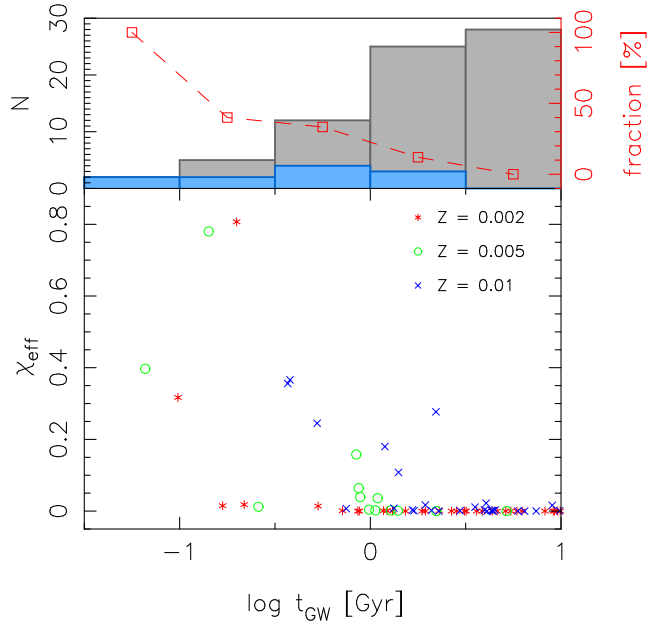


Figure 3. Same as Figure 2, but as a function of BBH merger time through gravitational wave radiation.

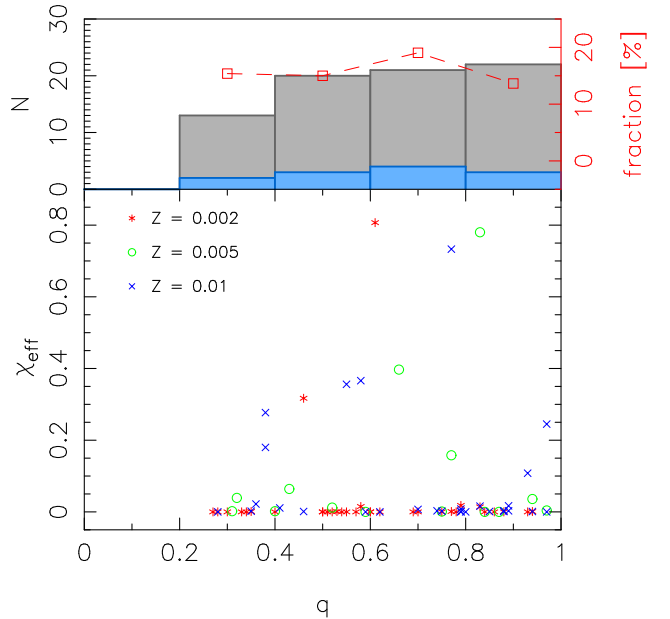


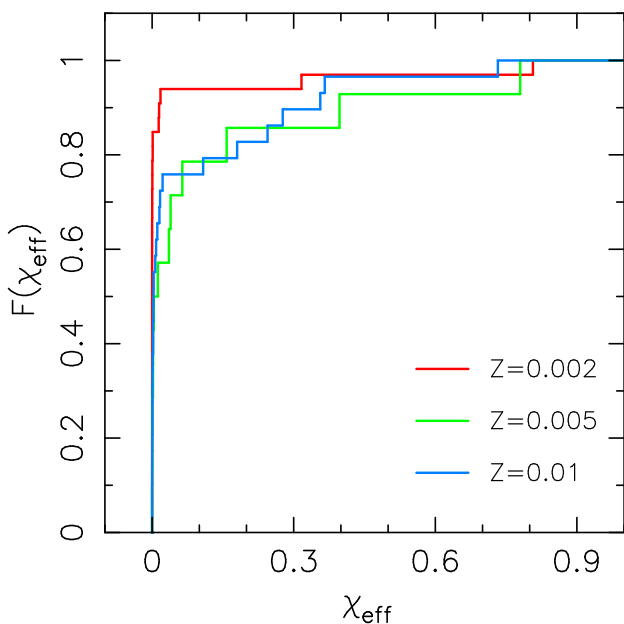
Figure 4. Same as Figure 2, but as a function of mass ratios of BBHs.

major axes after common envelope evolution, since binaries with lower-mass members need smaller binding energies (in absolute value) to shrink. WR stars in binaries with smaller semi-major axes are more tidally spun up as seen in equations (7) and (8).

A BBH with a smaller semi-major axis has a shorter merger time. This is consistent with the results shown in Figure 3, which shows that BBHs with shorter merger times tend to have larger spins. Figure 4 show that the fraction of BBHs with $\chi_{\text{eff}} > 0.1$ is independent on the mass ratio.

Table 2. Number of BBHs.

	N_{mBBH}^a	$N_{\text{mBBH}}(\chi_1 > 0.1)$	$N_{\text{mBBH}}(\chi_2 > 0.1)$	$N_{\text{mBBH}}(\chi_{\text{eff}} > 0.1)$
Model Z0002	37	1	2	2
Model Z0005	17	2	3	3
Model Z001	32	1	7	7
Model Z002	7	0	0	0

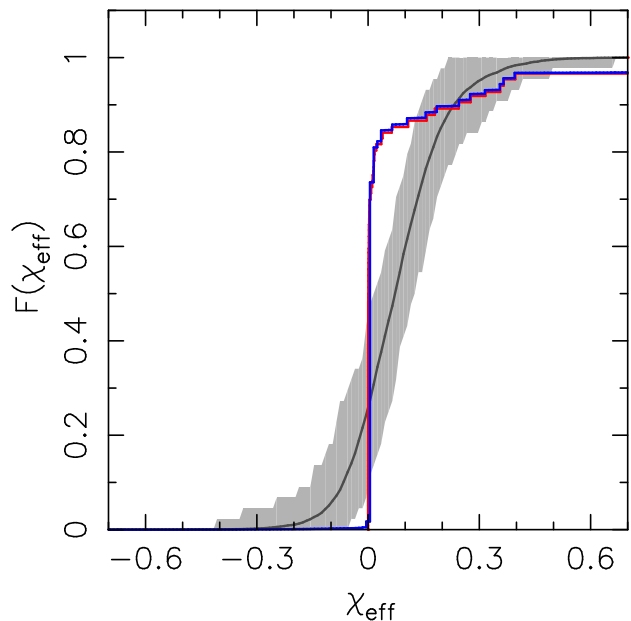
^a number of merging BBHs**Figure 5.** Cumulative distribution of effective spins of merging BBHs for each metallicity model in the case of the zero initial dimensionless spins model.

4.2 Spin distribution with the zero initial dimensionless spin

Figure 5 shows the cumulative distribution of effective spins, $F(\chi_{\text{eff}})$, for each metallicity model. For the 0.1 solar metallicity model (red line), the effective spin is almost zero for more than 90% of merging BBHs. For the 0.25 (green line), 0.5 (blue line) solar metallicity models, over 20% of the merging BBHs show larger effective spins than 0.1.

BBHs formed in more metal-rich clusters tend to get larger effective spins, since they have lower-mass BHs. For the solar-metallicity clusters, however, the effective spins of all merging BBHs are almost zero. This is because most of these BBHs experienced a three-body interaction and shrank their orbits to become merging BBHs (See Paper II). Although some of BBHs are formed via common envelope evolution, the resulting BBH progenitors have too large separations to be spun up through tidal interactions. For the solar-metallicity clusters, stars lose a large part of their envelopes due to strong stellar winds before they experience common envelope evolution.

In order to calculate the local merger rate density, we have obtained the cosmic star formation history for our four metallicity model from the observation (Chruslinska & Nelemans 2019) in Paper II (See also Figure 8 of Paper II). Using the cosmic star formation

**Figure 6.** The cumulative local distribution of the effective spins in the case of the zero initial dimensionless spins model. The red line shows the result obtained from our simulations. The blue line indicates the effective spin distribution, taking into account spin tilt by single encounters after BBH formations. The solid black line shows the one estimated from gravitational wave detection (see also Figure 24. of The LIGO Scientific Collaboration et al. 2020). The grey region shows the central 98% credible bounds on the posterior predictive distributions.

history for each metallicity, we estimate the local spin distribution of merging BBHs.

The red line in Figure 6 shows the local spin distribution $F(\chi_{\text{eff}})$ obtained from our simulation. The grey region shows the central 98% credible bounds on the posterior predictive distributions (The LIGO Scientific Collaboration et al. 2020). Our results show that most of merging BBHs in the local Universe have zero effective spins. In these calculations, we assume that the initial dimensionless spins of WR stars just after common envelope evolution are zero. In Section 4.3, we consider WR stars which have non-zero spins tilt from the binary angular momentum vectors just after common envelope evolution.

We obtain the merger rate of BBHs with large effective spins. From the cumulative distribution in Figure 6, Therefore, about 16% of merging BBHs have effective spins larger than 0.1 in the local Universe. In Paper II, we have estimated that the local merger rate density of BBHs originated from the open clusters is about $70 \text{ yr}^{-1} \text{ Gpc}^{-3}$. Thus, the local merger rate density of BBHs with larger χ_{eff} than 0.1 is

$$R_{\chi_{\text{eff}} > 0.1} \sim 11 \text{ yr}^{-1} \text{ Gpc}^{-3}. \quad (13)$$

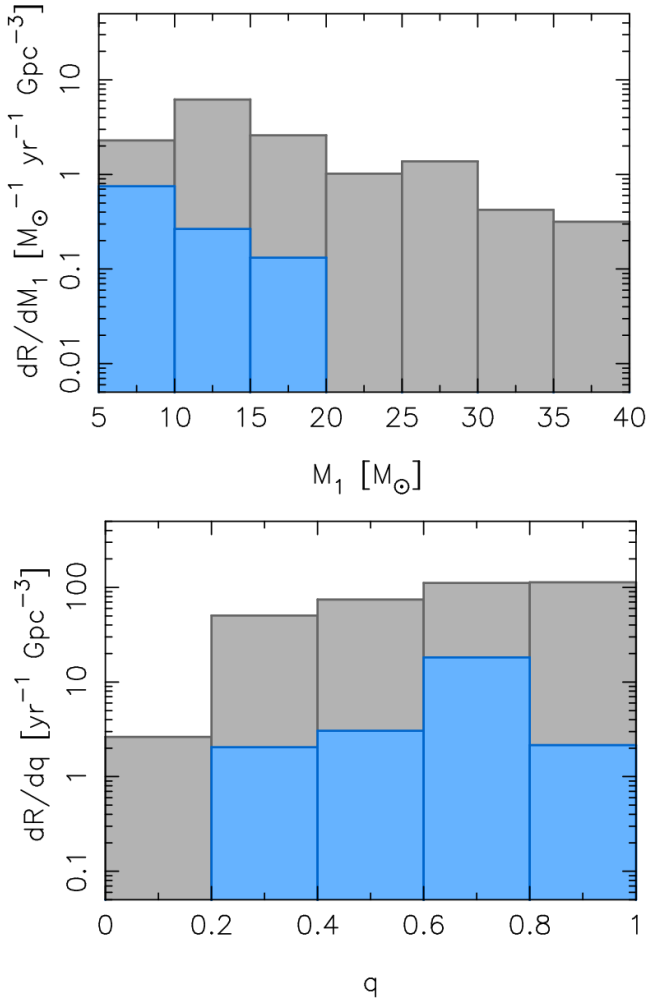


Figure 7. Differential merger rate density for primary BH masses, M_1 , (top panel) and mass ratios, q , (bottom panel) in the case of the zero initial dimensionless spins model. Grey and blue histograms show the differential merger rate density of BBHs with effective spins smaller and larger than 0.1, respectively.

It might seem odd that the local merger rate density of all the BBHs and BBHs with $\chi_{\text{eff}} > 0.1$ are, respectively, more than and comparable to the local merger rate density of all the BBHs inferred by gravitational observations (The LIGO Scientific Collaboration et al. 2020). Rather, our predicted merge rate density should be consistent with the observed one. This is because we ignore BH natal kicks via asymmetric supernova explosions, which decreases the local merger rate density of BBHs by several factors (Fujii et al. 2017).

Figure 7 shows the differential merger rate density for primary BH masses, M_1 , (top panel) and mass ratios q (bottom panel). The histograms with blue and grey areas are the differential local merger rate density expected from our simulations (the same as Figure 9 in Paper II). The blue area is the differential local merger rate density when we focus only on BBHs with $\chi_{\text{eff}} > 0.1$. As shown in Figure 2, BBHs with lower primary masses tend to have larger spins.

Finally, we investigate the effect of dynamical interactions of merging BBHs with other BHs. As Trani et al. (2021) found, $\sim 10\%$ of merging BBHs with moderately spinning BHs can experience single dynamical interactions with other BHs in open clusters until they merge, or are ejected from open clusters. Then, such interac-

tions should cause spin-orbit misalignments, and change the effective spin distribution. Using the misalignment distribution of the case with open cluster (OC) and $Z = 0.002$ (see the green dashed curve in the middle panel of Fig. 2 in Trani et al. (2021)), we modify the effective distribution as seen in the blue curve in Figure 6. Since there are many BBHs with $\chi_{\text{eff}} = 0$, the distribution is still not in good agreement with the observed one. However, the distribution may be more probable. This is because BBHs with negative χ_{eff} appear, and there are still more BBHs with positive χ_{eff} than with negative χ_{eff} .

4.3 Spin distribution with the flat isotropic model

Figure 6 shows that χ_{eff} is equal to zero for many BBHs. This is because initial dimensionless spins was assumed to be zero for all WR stars just after common envelope evolution. Therefore, all BBHs without tidally spun up show $\chi_{\text{eff}} = 0$. In this subsection, we assume the flat isotropic model for the initial dimensionless spins (see section 3). We denote $\chi_*(0)$ of primary and secondary WR stars by $\chi_{*,1}(0)$ and $\chi_{*,2}(0)$, respectively. 20 samples of $\chi_{*,1}(0)$ and $\chi_{*,2}(0)$ are randomly assigned to each binary formed in the simulation, and the final χ_{eff} is calculated. For the BBHs dynamically assembled from isolated BHs, which do not experience common envelope evolution, we assume that the stellar dimensionless spins are uniformly distributed between 0 and 1 at the formation time, and calculate the subsequent spin evolution. Naturally, the tidal spin-up effect does not affect isolated WR stars, and only the spin loss due to the stellar wind is calculated. We also assume that the spin angular momentum vector is randomly oriented when the binary is formed by dynamical interaction.

Figure 8 shows the cumulative distribution of χ_{eff} of merging BBHs with the flat isotropic model for the initial dimensionless spins with $t_w = 0.5, 1.0$ and 3.0 Myr. In the case of shorter t_w , more spin angular momentum is lost during the evolution from WR to BH than the case of longer t_w . Therefore, for models with smaller t_w , χ_{eff} is more concentrated around zero.

In Figure 9, we present the same plot as Figure 6, but in the case of the flat isotropic model for the initial dimensionless spins with $t_w = 0.5, 1.0$ and 3.0 Myr. By considering the flat isotropic model for the initial dimensionless spins, the χ_{eff} is distributed around zero and slightly biased to the positive side due to the effect of the tidal spin-up. This distribution is similar to the one estimated from gravitational wave observation (The LIGO Scientific Collaboration et al. 2020).

We investigate the dependence of the cumulative distribution on the primary mass. Figure 10 shows the cumulative distribution of χ_{eff} for the merging BBHs with some primary mass ranges. BBHs with smaller primary masses have larger effective spins. This is because BBHs with smaller primary masses tend to have larger effective spins, as shown in Figure 2. This may be consistent with a negative correlation between BBH masses and effective spins which Safarzadeh et al. (2020) have shown, using the data of the first and second observing runs of LIGO and Virgo.

5 CONCLUSIONS

We performed direct N-body simulations of open clusters with a mass of $2500 M_\odot$ and four different metallicity models ($Z = 0.1, 0.25, 0.5, 1.0 Z_\odot$). We investigated the spin evolution of WR stars tidally spun-up by their close companions, which evolve to

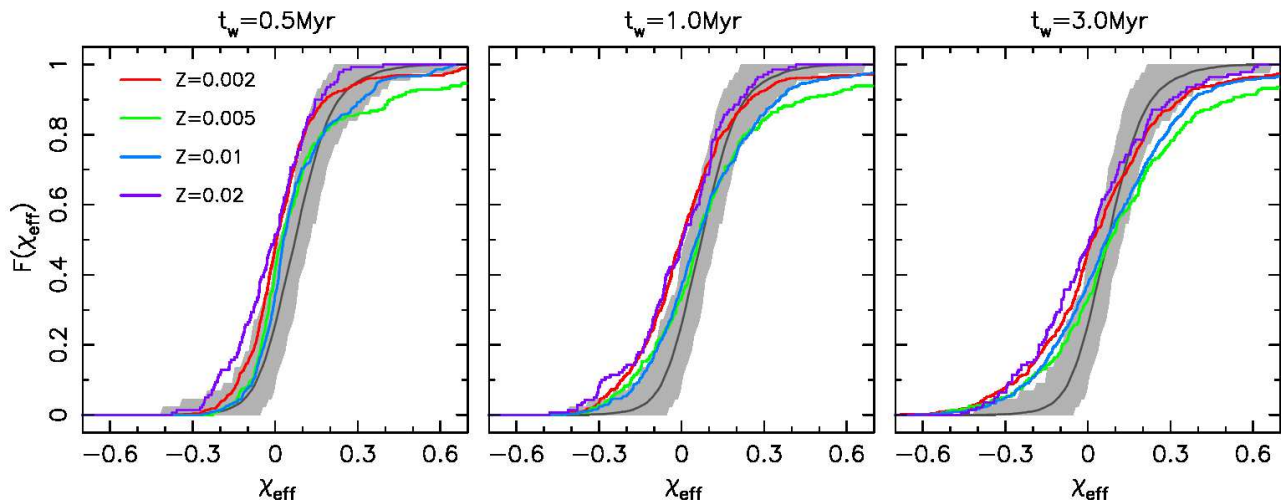


Figure 8. Same as Figure 5, but in the case of the flat isotropic model for $\chi_*(0)$ with $t_w = 0.5, 1.0$ and 3.0 Myr from left to right panel.

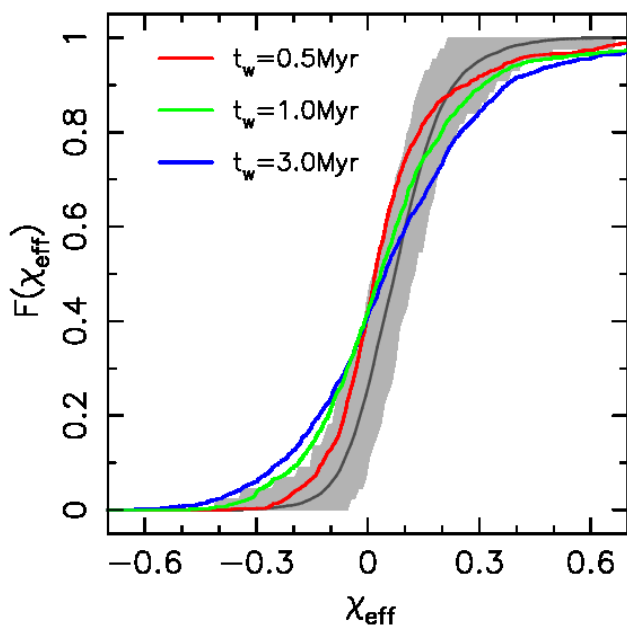


Figure 9. Same as Figure 6, but in the case of the flat isotropic model for $\chi_*(0)$ with $t_w = 0.5, 1.0$ and 3.0 Myr.

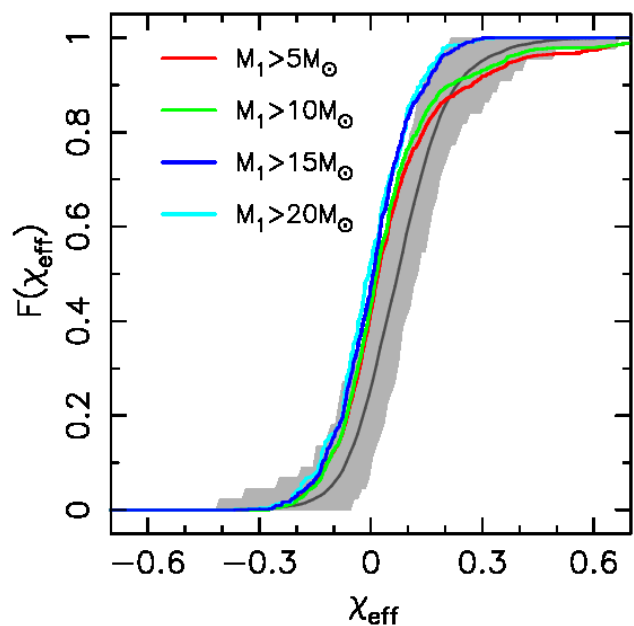


Figure 10. Same as case of $t_w = 0.5$ Myr in Figure 9, but results obtained from different primary masses range.

BBHs as the sources of gravitational waves. As a result, we found the following:

(i) Some of the BBHs with small semi-major axes have greater effective spins than 0.1 because of strong tidal forces from the companions, even assuming that BH progenitors have zero spins immediately after common envelope evolution.

(ii) BBHs have larger effective spins in more metal-rich clusters except for the solar-metallicity clusters. More metal-rich clusters form lower-mass BHs due to stellar wind mass loss, and lower-mass BHs have tighter WR stars just after common envelope evolution. The WR stars are more tidally spun-up by the BHs. In the solar-metallicity clusters, most of merging BBHs are formed not through common envelope evolution, but through dynamical interactions.

(iii) We estimated the effective spin distribution of merging

BBHs formed in open clusters as gravitational wave sources. We found that about 16% of local merging BBHs have effective spins larger than 0.1. Hence, the local merger rate density of BBHs with χ_{eff} larger than 0.1 is $\sim 11 \text{ yr}^{-1} \text{ Gpc}^{-3}$, if we adopt $\sim 70 \text{ yr}^{-1} \text{ Gpc}^{-3}$ for the local merger rate density of all the BBHs as described in Paper II.

(iv) Considering the flat isotropic distribution of dimensionless spins for WR stars just after common envelope evolution, the distribution of χ_{eff} extends around zero and is slightly biased to the positive side due to the effect of tidal spin-up of BH progenitors. This distribution is similar to the one inferred from gravitational wave observations (The LIGO Scientific Collaboration et al. 2020).

Future observations of gravitational waves, which will provide information on the spin of BBHs, especially those of small masses,

will allow us to discuss in detail the spin evolution mechanism of BBHs in open clusters.

ACKNOWLEDGMENTS

This work is supported by JSPS KAKENHI Grant Number 17H06360, 19H01933, and 19K03907 and The University of Tokyo Excellent Young Researcher Program, and MEXT as “Program for Promoting Researches on the Supercomputer Fugaku” (Toward a unified view of the universe: from large scale structures to planets, Revealing the formation history of the universe with large-scale simulations and astronomical big data). Numerical calculations reported in this paper were supported by Initiative on Promotion of Supercomputing for Young or Women Researchers, Supercomputing Division, Information Technology Center, The University of Tokyo.

REFERENCES

- Aarseth S. J., 1999, *PASP*, **111**, 1333
 Abbott B. P., et al., 2019a, *Physical Review X*, **9**, 031040
 Abbott B. P., et al., 2019b, *ApJ*, **882**, L24
 Abbott R., et al., 2020, arXiv e-prints, p. arXiv:2010.14527
 Antonini F., Gieles M., 2020, *MNRAS*, **492**, 2936
 Antonini F., Rasio F. A., 2016, *ApJ*, **831**, 187
 Arca Sedda M., 2020, *ApJ*, **891**, 47
 Arca-Sedda M., Capuzzo-Dolcetta R., 2019, *MNRAS*, **483**, 152
 Askar A., Szkudlarek M., Gondek-Rosińska D., Giersz M., Bulik T., 2017, *MNRAS*, **464**, L36
 Bae Y.-B., Kim C., Lee H. M., 2014, *MNRAS*, **440**, 2714
 Banerjee S., 2017, *MNRAS*, **467**, 524
 Banerjee S., 2018a, *MNRAS*, **473**, 909
 Banerjee S., 2018b, *MNRAS*, **481**, 5123
 Banerjee S., 2021, *MNRAS*, **500**, 3002
 Banerjee S., Baumgardt H., Kroupa P., 2010, *MNRAS*, **402**, 371
 Bavera S. S., et al., 2020, *A&A*, **635**, A97
 Belczynski K., Bulik T., Fryer C. L., Ruitter A., Valsecchi F., Vink J. S., Hurley J. R., 2010, *ApJ*, **714**, 1217
 Belczynski K., Holz D. E., Bulik T., O’Shaughnessy R., 2016, *Nature*, **534**, 512
 Belczynski K., et al., 2020, *A&A*, **636**, A104
 Bethe H. A., Brown G. E., 1998, *ApJ*, **506**, 780
 Bouffanais Y., Mapelli M., Gerosa D., Di Carlo U. N., Giacobbo N., Berti E., Baibhav V., 2019, *ApJ*, **886**, 25
 Chruslinska M., Nelemans G., 2019, *MNRAS*, **488**, 5300
 Di Carlo U. N., Giacobbo N., Mapelli M., Pasquato M., Spera M., Wang L., Haardt F., 2019, *MNRAS*, **487**, 2947
 Dominik M., Belczynski K., Fryer C., Holz D. E., Berti E., Bulik T., Mandel I., O’Shaughnessy R., 2012, *ApJ*, **759**, 52
 Downing J. M. B., Benacquista M. J., Giersz M., Spurzem R., 2010, *MNRAS*, **407**, 1946
 Downing J. M. B., Benacquista M. J., Giersz M., Spurzem R., 2011, *MNRAS*, **416**, 133
 Fujii M. S., Portegies Zwart S., 2014, *MNRAS*, **439**, 1003
 Fujii M. S., Tanikawa A., Makino J., 2017, *PASJ*, **69**, 94
 Giacobbo N., Mapelli M., Spera M., 2018, *MNRAS*, **474**, 2959
 Goswami S., Kiel P., Rasio F. A., 2014, *ApJ*, **781**, 81
 Gürkan M. A., Freitag M., Rasio F. A., 2004, *ApJ*, **604**, 632
 Hamers A. S., Bar-Or B., Petrovich C., Antonini F., 2018, *ApJ*, **865**, 2
 Hoang B.-M., Naoz S., Kocsis B., Rasio F. A., Dosopoulou F., 2018, *ApJ*, **856**, 140
 Hoang B.-M., Naoz S., Kocsis B., Farr W. M., McIver J., 2019, *ApJ*, **875**, L31
 Hong J., Vesperini E., Askar A., Giersz M., Szkudlarek M., Bulik T., 2018, *MNRAS*, **480**, 5645
 Hotokezaka K., Piran T., 2017, *ApJ*, **842**, 111
 Hurley J. R., Pols O. R., Tout C. A., 2000, *MNRAS*, **315**, 543
 Kinugawa T., Inayoshi K., Hotokezaka K., Nakauchi D., Nakamura T., 2014, *MNRAS*, **442**, 2963
 Kremer K., et al., 2020, *ApJS*, **247**, 48
 Kroupa P., 2001, *MNRAS*, **322**, 231
 Kumamoto J., Fujii M. S., Tanikawa A., 2019, *MNRAS*, **486**, 3942
 Kumamoto J., Fujii M. S., Tanikawa A., 2020, *MNRAS*, **495**, 4268
 Kushnir D., Zaldarriaga M., Kollmeier J. A., Waldman R., 2017, *MNRAS*, **467**, 2146
 Kustaanheimo P., Stiefel E., 1965, *Journal für die reine und angewandte Mathematik*, **218**, 204
 Makino J., Aarseth S. J., 1992, *PASJ*, **44**, 141
 Mapelli M., 2016, *MNRAS*, **459**, 3432
 Marks M., Kroupa P., 2010, *MNRAS*, **406**, 2000
 McKernan B., et al., 2018, *ApJ*, **866**, 66
 Mikkola S., Aarseth S. J., 1993, *Celestial Mechanics and Dynamical Astronomy*, **57**, 439
 Morscher M., Umbreit S., Farr W. M., Rasio F. A., 2013, *ApJ*, **763**, L15
 O’Leary R. M., Rasio F. A., Fregeau J. M., Ivanova N., O’Shaughnessy R., 2006, *ApJ*, **637**, 937
 O’Leary R. M., Kocsis B., Loeb A., 2009, *MNRAS*, **395**, 2127
 Park D., Kim C., Lee H. M., Bae Y.-B., Belczynski K., 2017, *MNRAS*, **469**, 4665
 Piran Z., Piran T., 2020, *ApJ*, **892**, 64
 Plummer H. C., 1911, *MNRAS*, **71**, 460
 Portegies Zwart S. F., McMillan S. L. W., 2000, *ApJ*, **528**, L17
 Portegies Zwart S. F., McMillan S. L. W., Gieles M., 2010, *ARA&A*, **48**, 431
 Rastello S., Amaro-Seoane P., Arca-Sedda M., Capuzzo-Dolcetta R., Fragione G., Tosta e Melo I., 2019, *MNRAS*, **483**, 1233
 Rodriguez C. L., Morscher M., Pattabiraman B., Chatterjee S., Haster C.-J., Rasio F. A., 2015, *Physical Review Letters*, **115**, 051101
 Rodriguez C. L., Chatterjee S., Rasio F. A., 2016, *Phys. Rev. D*, **93**, 084029
 Sadowski A., Belczynski K., Bulik T., Ivanova N., Rasio F. A., O’Shaughnessy R., 2008, *ApJ*, **676**, 1162
 Safarzadeh M., Farr W. M., Ramirez-Ruiz E., 2020, *ApJ*, **894**, 129
 Tagawa H., Haiman Z., Kocsis B., 2020, *ApJ*, **898**, 25
 Tanikawa A., 2013, *MNRAS*, **435**, 1358
 Tanikawa A., Susa H., Yoshida T., Trani A. A., Kinugawa T., 2020a, arXiv e-prints, p. arXiv:2008.01890
 Tanikawa A., Kinugawa T., Yoshida T., Hijikawa K., Umeda H., 2020b, arXiv e-prints, p. arXiv:2010.07616
 The LIGO Scientific Collaboration et al., 2020, arXiv e-prints, p. arXiv:2010.14533
 Tout C. A., Aarseth S. J., Pols O. R., Eggleton P. P., 1997, *MNRAS*, **291**, 732
 Trani A. A., 2020, in Bragaglia A., Davies M., Sills A., Vesperini E., eds, Vol. 351, *Star Clusters: From the Milky Way to the Early Universe*. pp 174–177 (arXiv:1908.07535), doi:10.1017/S174392131900721X
 Trani A. A., Tanikawa A., Fujii M. S., Leigh N. W. C., Kumamoto J., 2021, arXiv e-prints, p. arXiv:2102.01689
 Tutukov A., Yungelson L., Klayman A., 1973, *Nauchnye Informatsii*, **27**, 3
 Wang L., Spurzem R., Aarseth S., Nitadori K., Berczik P., Kouwenhoven M. B. N., Naab T., 2015, *MNRAS*, **450**, 4070
 Wang L., Fujii M. S., Tanikawa A., 2021, arXiv e-prints, p. arXiv:2101.09283
 Zevin M., Samsing J., Rodriguez C., Haster C.-J., Ramirez-Ruiz E., 2019, *ApJ*, **871**, 91
 Ziosi B. M., Mapelli M., Branchesi M., Tormen G., 2014, *MNRAS*, **441**, 3703

This paper has been typeset from a $\text{\TeX}/\text{\LaTeX}$ file prepared by the author.